Exciton Bleaching and Ultrafast Electron Cooling in Anatase TiO_2 Nanoparticles Revealed by Two-Dimensional Deep-Ultraviolet Spectroscopy

Edoardo Baldini,[1] Tania Palmieri,[1] Enrico Pomarico,[1] Gerald Auböck,[1] and Majed Chergui[1]

[1]*Laboratory of Ultrafast Spectroscopy, ISIC and Lausanne Centre for Ultrafast Science (LACUS), École Polytechnique Fédérale de Lausanne, CH-1015 Lausanne, Switzerland*

(Dated: July 19, 2022)

Abstract

The recent unravelling of strongly bound excitons in anatase TiO_2 nanoparticles at room temperature has shed light on the importance of many-body effects in samples used for applications. Here, we demonstrate the interplay between many-body interactions and correlations in highly-excited anatase TiO_2 nanoparticles by means of ultrafast two-dimensional deep-ultraviolet spectroscopy. We observe that the exciton optical nonlinearities upon non-resonant excitation are dominated by phase-space filling and long-range Coulomb screening, reflecting the dynamics of the photoexcited electron density. By tracking the renormalization of the exciton feature over time, we unveil the timescales involved in the intraband hot electron thermalization. We observe that the strong electron-phonon coupling results in an ultrafast dissipation of the electronic excess energy within 50 fs. Our findings open new perspectives in the design of alternative resonant excitation schemes to be tested in photocatalysis and nanotechnology.

In the last decades, anatase TiO_2 has attracted huge interest as one of the most promising materials for a variety of challenging applications, ranging from photocatalysis [1, 2] to photovoltaics [3]. Key to these technologies is a deep knowledge of the nature, dynamics and transport of the photogenerated/injected charge carriers, which in turn depend on the details of the electronic structure and the emergence of many body-effects. Since anatase TiO_2 is a d^0 transition metal oxide (TMO), strong electron-electron correlations do not play a substantial role in the electronic structure [4]. Hence, this solid can be classified within the simple band insulator scheme, in which the forbidden energy gap arises as a result of band theory and it is not a consequence of the strong on-site Coulomb interaction. However, different to other conventional band insulators, anatase TiO_2 represents a peculiar example in which electron-phonon interaction and electron-hole correlation become relatively strong and concur to influence the optical spectra. On the one hand, the presence of a moderately large electron-phonon coupling in anatase TiO_2 has often been invoked to interpret experimental results naturally pointing to the polaronic (self-trapped) picture [5–11]. Notable examples include the low temperature green photoluminescence (PL) due to intrinsically self-trapped excitons [12–18] and the room temperature (RT) electron mobilities whose values are limited by strong scattering with phonons [8]. On the other hand, the role of many-body correlations has been thought to be negligible in this material and, as such, it remained widely unexplored. Only recently, by employing state-of-the-art experimental [19] and computational techniques [19–23], have electron-hole Coulomb correlations been demonstrated to play a substantial role in anatase compared to the rutile polymorph, leading to the emergence of bound direct excitons on the continuum of indirect interband transitions. These excitons are characterized by a binding energy exceeding 150 meV and are expected to possess a strong coupling to the phonon degrees of freedom. Clear manifestation of this behaviour is the persistence of a broad exciton linewidth even at the lowest temperatures in high-quality single crystals [19], which emerges as a consequence of multiple phonon sidebands coupled to the collective exciton state and do not reflect the characteristic exciton lifetime [24]. As a result, these excitons are notably very robust with respect to temperature, but also to sample quality, clearly appearing in the defect-rich samples used for RT applications [19]. With respect to the excitonic features, conventional nanosystems such as TiO_2 nanoparticles (NPs) with radii of 5-15 nm behave similarly to the bulk, as the exciton Bohr radius (3.2 nm) rules out quantum confinement effects [19]. This implies that the electronic properties

of anatase TiO_2 nanosystems can be analyzed within the framework of the bulk material band structure.

Since the relative importance of interactions and correlations in anatase TiO_2 is a very recent topic, one would expect a pronounced influence on the carrier dynamics even in nano-sized systems. These processes are indeed predicted to govern the timescales for intraband carrier cooling via phonon emission [11] and they can also influence the material optical properties offering strong optical nonlinearities. As such, they are of pivotal importance for the design and optimization of novel devices. This calls for the search of related spectroscopic observables that have not been detected in the ultrafast dynamics of this widely used TMO. Indeed, ultrafast broadband optical spectroscopy has been extensively performed to monitor the change in the material absorption over a wide spectral range from the far-infrared to the visible [25–31]. In these studies, the photoexcited electrons and holes in the system were treated as uncorrelated, an approximation that is valid only when the pump photons are non-resonant with the newly discovered excitons. Under these conditions, above-gap photoexcitation triggers a pronounced redistribution of the material spectral weight from high- to low-energies, leading to the emergence of a free-carrier Drude response and of absorption features attributed to localized charges trapped at impurity and defect centres [25–30]. Although these studies provided valuable details on the electron-hole recombination pathways, they put strong emphasis on surface effects and the reduced dimensionality of the nanosized systems, losing track of the material electronic structure. For example, due to the simultaneous contribution of free-electrons and free-holes in the system, the transient spectra possess a high degree of ambiguity, thus hindering a clear distinction between the carriers and complicating the study of many-body phenomena. More insightful information was provided by time-resolved PL, which revealed the strongly Stokes-shifted radiative recombination of self-trapped excitons [13–18]. However, these processes were found to emerge only at low temperatures and to disappear under the typical conditions of applications. Furthermore, only long timescales (> 20 ps) were investigated.

To find signatures of interactions and correlations, a superior method relies on combining sub-100 fs temporal resolution and broad detection window for transient absorption (ΔA) in the deep-ultraviolet (UV) [32], which has so far been inaccessible to previous ultrafast studies. With the use of deep-UV continuum probe pulses, one gains direct access to the region in which the spectral weight is removed after above-gap excitation and the excitonic

features become clearly distinguishable. Insightful information on single-particle and many-body effects is encoded in the bleaching of the exciton state, a nonlinear optical effect that depends on the presence of all the particles in the material [33, 34].

Most prominent sources of excitonic optical nonlinearities are: i) Phase-space filling (PSF), which causes a reduction in the exciton oscillator strength by decreasing the number of single-particle states contributing to the exciton; ii) long-range Coulomb screening (CS), which broadens the exciton band and shifts it to the blue, as the photoexcited carrier density screens the electron-hole interaction and reduces the exciton binding energy; iii) bandgap renormalization (BGR), which leads to a density-dependent shrinkage of the single-particle states (and consequently of the exciton states), and may reduce the exciton oscillator strength. These processes act simultaneously on the exciton lineshapes, their relative weights being governed by the material parameters and dimensionality [33, 34].

Here, we reveal the hierarchy of phenomena at the origin of the exciton nonlinearities in highly-excited anatase TiO_2 NPs by tracking the exciton renormalization via ultrafast two-dimensional (2D) deep-UV spectroscopy. We observe that PSF of the CB states by the photoexcited electron density represents the major mechanism at play upon light generation of uncorrelated electron-hole pairs. This allows us to address a subject that has remained elusive over time, namely the timescales involved in the intraband hot electron thermalization in a nanosized anatase TiO_2 system. We observe the occurrence of an ultrafast electron cooling within 50 fs, compatible with phonon-mediated relaxation processes in the strong coupling regime. Our findings unveil previously undetected details of the carrier dynamics in this TMO and open new perspectives for the design of excitation schemes in photocatalysis and nanotechnology.

Results and Discussion

The experimental procedures are described in §§ S1-S2. In our first experiment, we vary the pump photoexcitation between 4.00 eV and 4.60 eV and simultaneously monitor ΔA over a broad spectral range covering the excitonic resonances (3.50 - 4.60 eV). The time resolution of this data set is 150 fs and the photoexcited carrier density is $n = 5.6 \times 10^{20}$ cm^{-3}. This high-excitation density regime is chosen to avoid the emergence of polaronic effects within the bands and promote the formation of a mobile electron-hole liquid [9].

Figure 1(a) shows ultrafast 2D deep-UV pump-probe colour-coded maps at different time delays (1 ps, 100 ps and 500 ps). The straight line in each map indicates the region in which pump and probe have the same photon energy. This spectral range is affected by artefacts caused by the scattering of the pump beam into the spectrometer. All transients are characterized by a negative signal over the entire probe spectral range, in which two long-lived features are clearly distinguished at a probe photon energy of 3.88 eV and 4.35 eV. While the former excitation is present at all pump photon energies, the latter becomes more prominent when the pump is tuned above 4.10 eV. Further insights into the evolution of the ΔA spectrum for different pump photon energies is obtained from the cuts of the map in Fig. 1(a) at 1 ps along the probe photon energy axis. The selected transient spectra are shown in Fig. 1(b), normalized with respect to the absolute maximum of the feature peaking at 3.88 eV. For comparison, also the inverted steady-state absorption spectrum ($-A$) of the same colloidal solution of anatase TiO_2 NPs is displayed (black curve). We observe that both features appearing in the ΔA spectra retain a well-defined Lorentzian lineshape with a width of $\sim$300 meV, in contrast to the featureless steady-state spectrum. Moreover, no apparent shift of the low-energy Lorentzian peak is detected when the pump photon energy is varied. Clear information on the peak of the high-energy feature cannot be retrieved due to the influence of the pump beam scattering. The features at 3.88 eV and $\sim$ 4.35 eV are assigned to the a- and c-axis bound excitons of anatase TiO_2, respectively, as discussed in Ref. [19]. Both excitons are observed in the ultrafast response of anatase TiO_2 NPs due to the random orientation of the nanocrystals in solution. These bands are hidden in the steady-state absorption spectrum [35] due to the strong scattering of light. They become apparent in the pump-probe transient absorption spectrum because the scattered light is canceled out.

From Fig. 1 we can already draw an important conclusion on the nonequilibrium dynamics of anatase TiO_2 NPs, which was neglected in all previous studies. Depending on the choice of the pump photon energy, one can create uncorrelated electron-hole pairs (non-resonant excitation) or excitons (resonant excitation). In the former case, the pump photon energy determines the regions of the Brillouin zone (BZ) where the nonequilibrium electron-hole density is created. This consideration acquires even more importance in an indirect bandgap insulator as anatase TiO_2, since the pump photon energy can also be tuned to excite phonon-assisted interband transitions (despite their lower cross section). On the con-

trary, resonant excitation leads to the creation of bound exciton species in the system, which complicates the interpretation of the ultrafast dynamics due to the presence of many-body exciton-exciton interactions.

Here, we focus on the non-resonant excitation and clarify the impact of uncorrelated electron-hole pairs on the bound exciton feature. The effects produced upon resonant excitation will be addressed in a future work. To this end, we select one data set from the ultrafast 2D deep-UV spectroscopy maps shown in Fig. 1, namely the one in which the pump photon energy is 4.05 eV. Since this pump photon energy lies below the c-axis exciton peak [19], it is expected to minimize the c-axis contribution to the ΔA response. This, in turn, allows us to anchor more accurately the resulting ultrafast dynamics into the details of the electronic structure. The data are displayed in Fig. 2(a) as a colour-coded map of ΔA as a function of probe photon energy and time delay between pump and probe. As expected, the spectral response shows the long-lived feature of the a-axis exciton peaking at 3.88 eV, followed by the weaker shoulder of the c-axis exciton around 4.35 eV. We first investigate how the exciton spectrum evolves as a function of time. The results are shown in Fig. 2(b), which displays the ΔA spectrum at different time delays. The normalization of the ΔA spectra with respect to the peak of the dominant feature (Fig. S2) reveals that this peak does not shift during the relaxation dynamics. Complementary insights into the ultrafast dynamics is offered by the analysis of the temporal traces in the vicinity of the excitonic features. In Fig. 2(c), we present the evolution of the ΔA signal, by cutting three traces at specific probe photon energies below (3.77 eV), in correspondence to (3.90 eV) and above (4.10 eV) the a-axis exciton peak. All temporal traces exhibit a resolution-limited rise of 150 fs, followed by a long-lived decay persisting beyond 1 ns. On top of this incoherent response, a low-frequency oscillation modulates the whole spectrum during the first 5 ps and undergoes a dramatic damping after one oscillation. This feature is due to the emergence of coherent acoustic phonons confined within the spherical TiO_2 NPs, which will be discussed elsewhere. Here, we retrieve the significant parameters of the incoherent response, by performing a global fit (GF) of ΔA as a function of time. We select thirteen temporal traces from the 3.60-4.15 eV range of the ΔA map (*i.e.* below the contribution of the c-axis exciton) and fit them simultaneously by imposing the same time constants. A satisfactory fit up to 1 ns can only be obtained with four exponential functions (with relaxation time τ) convoluted with a Gaussian accounting for the temporal duration of the pump pulse ($\sim$ 150

fs). From the GF, we obtain four time constants characterizing the recovery of the bleach: $\tau_1 = 1.60 \pm 0.12$ ps, $\tau_2 = 10 \pm 0.40$ ps, $\tau_3 = 50 \pm 1.70$ ps, $\tau_4 = 423 \pm 14.70$ ps. The results of the GF are shown as solid lines in Fig. 2(c), overlapped to the experimental data. The use of a GF enables us to disentangle the spectral dependence of the decay processes contributing to the recovery of the exciton bleach. The decomposition of the original ΔA spectrum into the different spectral components is provided in Fig. 2(d). The spectral dependence of the τ_1 and τ_2 relaxation components show a negative amplitude broader than the exciton lineshape, while the contributions of τ_3 and τ_4 decay processes affect mainly the exciton band. This suggests that the two faster decay processes have a different nature with respect to the two slower ones, recovering spectral weight in a broad region outside the exciton lineshape. All decay processes are strictly related to the electron-hole recombination mechanisms in the colloidal solution of anatase TiO_2 NPs, which reduce the density of delocalized carriers via radiative or non-radiative relaxation channels.

To identify the phenomena governed by the different time constants τ, one first needs to assess the relative weights of the optical nonlinearities contributing to the transient signal. With this respect, it is pivotal to clarify the electron-hole populations giving rise to the exciton collective state. Relying on the anatase TiO_2 band structure [21], the single-particle states contributing to the a-axis exciton lie along the Γ-Z direction of the BZ (Fig. 3). Due to symmetry of *p*-*d* wavefunctions, however, the states exactly at the Γ point are symmetry forbidden and do not contribute to the exciton state [21]. Once a nonequilibrium distribution of uncorrelated electron-hole pairs is created, the electrons are eventually expected to thermalize to the bottom of the CB at Γ and the holes to the top of the VB close to X. Since the deep-UV probe is sensitive to the joint density of states in the material, an induced transparency ($\Delta A < 0$) can arise from a density of electrons (holes) accumulated in the CB (VB) alone. In anatase TiO_2, the PSF contribution to the exciton bleaching is expected to arise only due to the presence of an electron population at the bottom of the CB. The hole contribution is absent, due to their ultimate relaxation to the top of the VB close at the X point. This consideration implies that PSF, long-range CS and BGR may all contribute to the observed optical nonlinearities. It is thus pivotal to address the effects related to the enhancement of the electronic screening upon pump photoexcitation. In this regard, we study how the exciton spectrum is renormalized as a function of the absorbed fluence upon photoexcitation at 4.05 eV, narrowing our detection range to cover only the spectral region

of the a-axis exciton. In this way, we can benefit from the higher stability of our setup and maintain the same experimental conditions over the time required for performing the fluence dependence. Within the explored fluence range, the signal scales linearly as a function of the absorbed fluence, thus ruling out the involvement of multiphoton absorption processes from the pump beam. The normalized spectra are shown in Fig. 4(a,b) for a delay time of 400 fs and 10 ps, respectively. On the one hand, the exciton lineshape is found to slightly broaden as the photoexcited carrier density is increased, suggesting the presence of long-range CS. On the other hand, we observe the absence of evident shifts in the peak energy position and of the derivative-like shapes typically retrieved in the presence of a substantial BGR. This implies perfect cancellation between the two distinct effects of CS and BGR even at such high carrier density. In general, the quantitative details of this compensation depend on both material and dimensionality [36]. From these measurements, we can conclude that the carrier density which is required to induce such dramatic changes of the exciton peak is higher than those produced by our photoexcitation. As a consequence, at sufficiently low electron-hole pair densities, when the continuum is still far from the resonances, only the loss of oscillator strength due to PSF and the broadening due to CS are apparent. These results further confirm the strongly bound exciton scenario for the a-axis exciton, in agreement with recent steady-state angle-resolved photoemission spectroscopy (ARPES), optical measurements and *ab initio* calculations demonstrating the ineffectiveness of BGR even for extremely high carrier densities ($n \sim 10^{20}$ cm^{-3}) [19]. Thus, we conclude that PSF and CS are the dominant effects contributing to the excitonic optical nonlinearities at our carrier densities. Consistent with this scenario, the exciton bleach is found to persist even when the pump photon energy is tuned at 3.54 eV, thus promoting indirect (phonon-assisted) interband transitions. On the contrary, when the NPs are photoexcited at 3.10 eV (even up to incident fluences of 34 mJ/cm^2), no signal is detected.

Establishing the dominant role played by CB electrons in blocking and screening the excitonic transitions allows one to retrieve valuable information on the electron recombination dynamics. Indeed, the ΔA signal at the excitonic resonance peak can be used as a measure of the photoexcited electron concentration changing with time. Representative temporal traces at a probe photon energy of 3.88 eV and for different excitation densities are shown in Fig. 4(c) and normalized with respect to their maximum. We observe that below 40 ps the bleach decay becomes faster as the fluence is increased, which is indica-

tive of higher-order recombination processes for the charge carriers such as bimolecular and Auger recombination. To explain this dependence, we recall that the recombination dynamics in band semiconductors and insulators proceeds via single-carrier nonradiative processes (trapping at impurity states), two-body radiative (bimolecular) mechanisms and nonradiative trap-Auger recombination process and three-body band-to-band Auger processes [37]. Since anatase TiO_2 is an indirect bandgap insulator, band-to-band radiative recombination is known to be extremely inefficient. Thus, the only radiative recombination pathways that can take place at RT are those involving a delocalized carrier in a band and a localized carrier trapped at a defect state. To verify the efficiency of the radiative recombination processes, we measure the ultrafast PL obtained in colloidal anatase TiO_2 NPs via femtosecond fluorescence up-conversion (see details in the SI). As the quantum yield for the RT PL in the first 100 ps is of the order of $\sim 1.3 \times 10^{-6}$, it is straightforward to assume that the recombination dynamics at early time delays in anatase TiO_2 is entirely governed by Auger mechanisms. This was already reported in the case of highly excited anatase TiO_2 NPs and thin films by transient absorption spectroscopy [25, 31]. It is also consistent with the spectral dependence of the τ_1 and τ_2 relaxation components (Fig. 2(d)), which retain a broad shape hinting to energetically redistributed carriers over a wider phase space during the Auger processes. In contrast, the longer τ_3 and τ_4 relaxation components can be assigned to electron trapping processes at defect states, which lead to a recovery of the bleach by emptying the phase space involved in the exciton state.

More interestingly, revealing the importance of PSF in the exciton bleaching process opens perspectives for addressing an aspect that has remained elusive over time, namely the timescale involved in the intraband cooling of the electrons to the bottom of the CB in anatase TiO_2 nanosystems. Recent *ab initio* calculations of the nonequilibrium electron dynamics estimated the time required for highly excited CB electrons to emit high-energy optical phonons and release their whole excess energy to be < 100 fs [11]. This was explained in relation to the strong electron-phonon coupling characterizing the material. A recent single-wavelength transient reflectivity experiment on rutile TiO_2 single crystals tracked the influence of carrier cooling onto the phase of the coherent A_g phonon mode at 74.4 meV, offering valuable information on the electron-phonon coupling dynamics [38]. Nevertheless, this method is blind to the details of the electronic structure and relies on the analysis of coherent optical phonons, whose observation in nanomaterials is not always straightforward.

Here, we circumvent these limitations by demonstrating the effectiveness of exciton bleaching as a probe of the intraband electron thermalization. To this aim, we focus on the rise of the exciton bleach signal by reducing the instrument response function of our setup to 80 fs. This implies shortening the duration of the pump pulses and flowing the colloidal solution as a free liquid jet to minimize detrimental effects of cross-phase modulation (CPM) around zero time delay (see Methods). In Fig. 5(a), the signal measured from anatase TiO_2 NPs at 3.88 eV and an excitation density $n \sim 2.1 \times 10^{20}$ cm^{-3} is compared with the signal observed from the solvent (acidic water) where the NPs are dissolved. In this way, artefacts due to residual CPM around t = 0 can be identified in the signal. Differences of amplitude between the traces reported in Fig. 5(a) are mainly due to the presence of a signal provided by the sample. The two traces cannot be directly subtracted, due to slightly different experimental conditions in the measurements. However, the instrument response function of the system is generally assumed to coincide with the duration of the CPM signal and can be represented by a Gaussian function (with a full-width at half-maximum of 80 fs) that envelops the CPM modulations (Fig. 5(a)). In Fig. 5(b) the ΔA from the anatase TiO_2 NPs unaffected by CPM is compared to three different decay functions convoluted with a Gaussian instrument response function of 80 fs. The three different functions consist of a variable rise time and an exponential decay. The upper limit to the rise time of the signal from anatase TiO_2 NPs is estimated by finding the highest value of the rise time at which the decaying function does not provide a good fit of the experimental points that are closer to time zero. From Fig. 3(b), this value is observed to be 50 fs, which is the upper limit to the rise of the exciton bleach and to the corresponding intraband electron cooling.

This value can be compared with predictions of *ab initio* calculations [11]. The total excess energy provided by the pump pulse has to be divided between the photoexcited electrons and holes. Momentum conservation results in the partition of the kinetic energy between electrons and holes according to the reciprocal ratio of their effective mass m_e^*/m_h^*, with the carrier having lower effective mass receiving more of excess energy

$$E_{\mathrm{exc}}^{\mathrm{e}}(\hbar\omega) = \frac{\hbar^2 k^2}{2m_e^*} = \frac{m_h^*}{m_e^* + m_h^*}\left(\hbar\omega - E_{\mathrm{gap}}\right) \tag{1}$$

$$E_{\mathrm{exc}}^{\mathrm{h}}(\hbar\omega) = \frac{\hbar^2 k^2}{2m_h^*} = \frac{m_e^*}{m_e^* + m_h^*}\left(\hbar\omega - E_{\mathrm{gap}}\right) \tag{2}$$

In our experiment, $\hbar\omega = 4.05$ eV and $E_{\rm gap} = 3.20$ eV. Rigorously, the electron and hole effective masses vary as a function of momentum k, being well-defined concepts only within the parabolic approximation for the band structure. From the inspection of the latter, we expect our pump photons to promote uncorrelated electron-hole pairs in the vicinity of the Γ point along the Γ-X direction (purple arrow in Fig. 3). Due to the high carrier densities involved in our experiment, we use the value of the electron effective mass reported by band theory $m_e^* = 0.42m_e$ (see §S5 for the choice of m_e^*) [39]. On the other hand, to provide an estimate of m_h^* from the details of the measured electronic structure, we rely on recent ARPES data for the top of the VB along the Γ-X direction in the case of an excess carrier density $n = 10^{19} \div 10^{20}$ cm^{-3} [19]. Performing a parabolic fit yields $m_h^* = 2.78m_e \pm 0.5m_e$, which also accounts for the polaronic contribution to the mass renormalization. The values of m_e^* and m_h^* lead to an excess energy repartition $E_{exc}^e \sim 0.74$ eV and $E_{exc}^h \sim 0.11$ eV. Under these conditions, following Ref. [11], we expect the timescale for emission of a single phonon by an excited carrier to be ∼2 fs and the total thermalization time to the CB edge ∼40 fs, in very good agreement with the < 50 fs for the rise of the bleach signal, suggesting that by then all the photoexcited electrons have already thermalized to the bottom of the CB (Fig. 3). On the other hand, the small excess energy received by the holes prevent them from undergoing rapid intervalley scattering to the X and Z side valley via emission of high-wavevector phonons. When the timescale obtained for the electron cooling in anatase TiO_2 is compared with the slower (> 250 fs) electron relaxation timescales retrieved in nonpolar indirect gap semiconductors, some conclusions can be drawn concerning the crucial role of the electron-phonon scattering channel in anatase. Indeed, in nonpolar materials (such as germanium and silicon) phonon scattering occurs through the optical phonon deformation potential interaction, while in partially-ionic polar systems (such as anatase TiO_2) the most effective coupling mechanism is represented by the electron-longitudinal optical (LO) phonon scattering described by the Fröhlich interaction [40]. The optical phonons that are most strongly coupled to the electronic degrees of freedom are those belonging to the branches of the E_u and A_{2u} modes [6, 9]. Due to this coupling, in the low carrier density limit, the CB electrons form well-defined large polaron quasiparticles, which then collapse into an electron liquid coupled to the phonon modes at high carrier densities. Within the single-particle limit probed by ARPES, the crossover is expected to take place around $n = 10^{19}$

cm^{-3} [9]. In the two-particle limit of optics, this threshold may be even lower, leading to the emergence of a well-defined Drude response for the photocarriers [31] instead of the characteristic absorption features of large polarons [41]. Even in this diffusive regime, the coupling between the electronic degrees of freedom and the phonons leads to an efficient and fast removal of electron excess energies larger than 0.2 eV, which are lost to the phonon bath within few tens of fs. In contrast, for excess energies less than the maximum LO phonon energy ($\sim$ 108 meV in TiO_2 [42]), constraints in the phonon phase space result in a dramatic decrease of the intraband cooling rate [43]. However, in this situation, as no excess energy is provided to the electronic system, no effective energy storage is obtained. These arguments lead us to conclude that, even in nanosized anatase TiO_2 systems, fast relaxation processes impose serious limitations to the practical use of the full photon energy in applications. This scenario is radically different from the physics of semiconductor quantum dots, in which the spacing between the discrete electronic levels is large enough to prevent fast phonon-mediated carrier cooling processes [44]. This calls for alternative excitation schemes to be used in anatase TiO_2. In this respect, a promising route involves the detailed investigation of resonant excitation of the strongly bound exciton species, in which the energy can be temporarily harvested. In particular, as the a-axis excitons are expected to move freely on the (001) plane [19, 21], these collective excitations may offer an efficient source to mediate the flow of energy at the nanoscale in engineered devices based on anatase TiO_2.

Conclusions

To conclude, in this work we provided first direct evidence of excitonic optical nonlinearities in anatase TiO_2 NPs at RT. Besides their importance for fundamental physics research, these excitons hold huge promise for future technological developments. Indeed, due to their sensitivity to the environment, they can be used as probes of ultrafast processes occurring in the material. Moreover, being stable species at RT, they offer great potential in the emerging field of excitonics. Here, we revealed selective information on the intraband and interband electron dynamics by tracking the renormalization of the excitonic features over time. We showed how, even in NPs, the strong electron-phonon coupling of the material results in short cooling timescales for electrons possessing a substantial (> 0.2 eV) excess energy. Under these conditions, any optical or acoustic phonon can be excited in the course

of the electron thermalization, thus contributing to a rapid loss of the electronic excess energy. This hinders the effective use of the excess energy of uncorrelated electron-hole pairs in devices based on nanosized TiO_2. More remarkably, our results highlight the importance of relating the carrier dynamics in anatase TiO_2 NPs to the details of the electronic structure, an aspect that was overlooked in all previous experimental studies, which mainly focused on the role of shallow and deep trap states at the surface of NPs. Finally, by unraveling the origin of the bound exciton bleaching in NPs, our findings pave the way to its application as a sensitive probe of carrier dynamics in a variety of nanosystems based on anatase TiO_2. Notable examples include modified forms of this material, such as the ones obtained upon chemical doping with magnetic ions or upon crystal structure control. In this respect, the ultimate goal would be to detect exciton bleaching in sensitized anatase TiO_2 surfaces, providing new insights into the interfacial electron transfer processes that regulate the efficiency of sensitized solar cells and photocatalytic reactions.

We acknowledge financial support from the Swiss NSF via the NCCR:MUST and the contracts No. 206021-157773, and 407040-154056 (PNR 70), the European Research Council Advanced Grant H2020 ERCEA 695197 DYNAMOX.

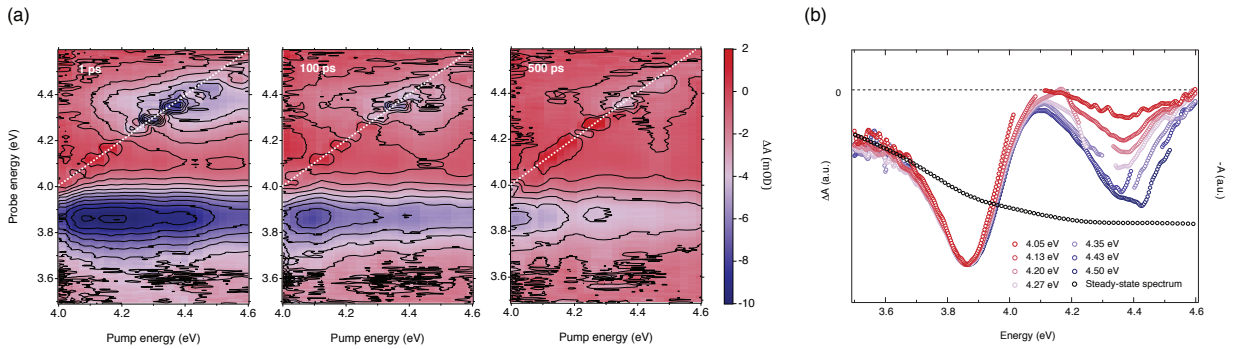

FIG. 1. (a) Colour-coded maps of ΔA measured via ultrafast 2D UV spectroscopy on a colloidal solution of anatase TiO_2 NPs at RT as a function of pump- and probe photon energy. The spectral response is displayed at three different time delays between pump and probe: 1 ps, 100 ps, 500 ps. The time resolution is estimated 150 fs and the photoexcited carrier density is $n = 5.6 \times 10^{20}$ cm^{-3}. (b) Normalized ΔA spectra at a fixed time-delay of 1 ps and for different pump photon energies (indicated in the figure). Each trace is normalized with respect to the minimum of the main feature at 3.88 eV. For comparison, the black trace shows the inverted ($-A$) steady-state absorption spectrum.

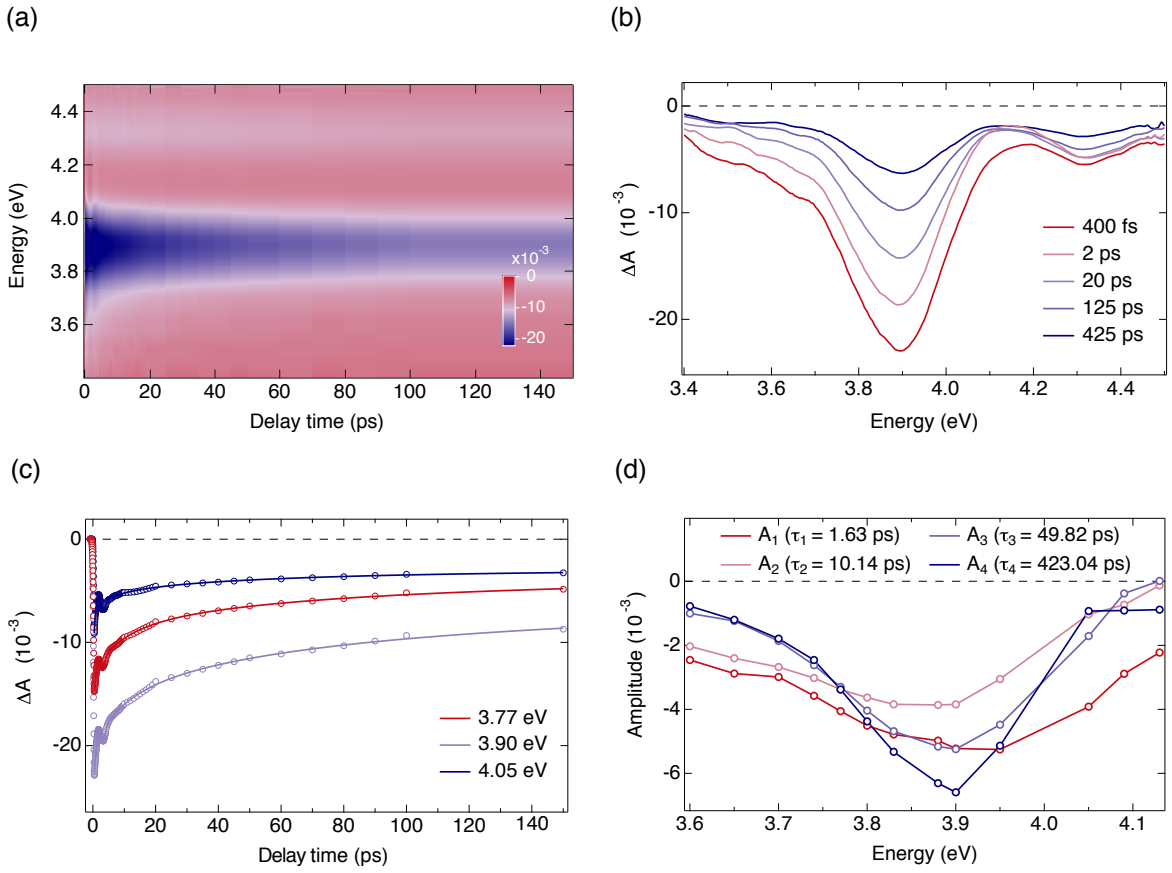

FIG. 2. (a) Colour-coded map of ΔA measured on a colloidal solution of anatase TiO_2 NPs as a function of probe photon energy and time delay between pump and probe. The time resolution is estimated 150 fs, the pump photon energy is set at 4.05 eV and the photoexcited carrier density is $n = 5.6 \times 10^{20}$ cm^{-3}. The dynamics are shown up to 150 ps. (b) ΔA spectra as a function of probe photon energy at representative delay times between pump and probe. (c) Experimental temporal traces of ΔA for different probe photon energies (dotted lines) and results of the global fit analysis (solid lines). (d) Contribution to ΔA response of the four relaxation components obtained from the global fit analysis.

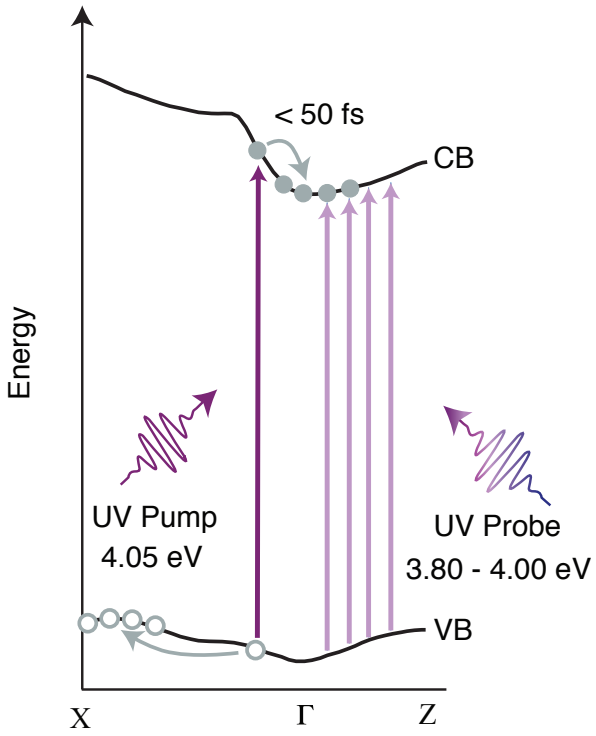

FIG. 3. Schematic representation of the deep-UV based detection of the ultrafast carrier dynamics in anatase TiO_2 NPs. The pump photon at 4.05 eV (purple arrow) excites electron-hole pairs through direct transitions. The broadband UV pulse (violet arrows) probes the exciton feature at 3.88 eV. The direct transitions contributing to this collective state lie along the Γ-Z region of the Brillouin zone. The band structure of anatase TiO_2 has been adapted from Ref. [21].

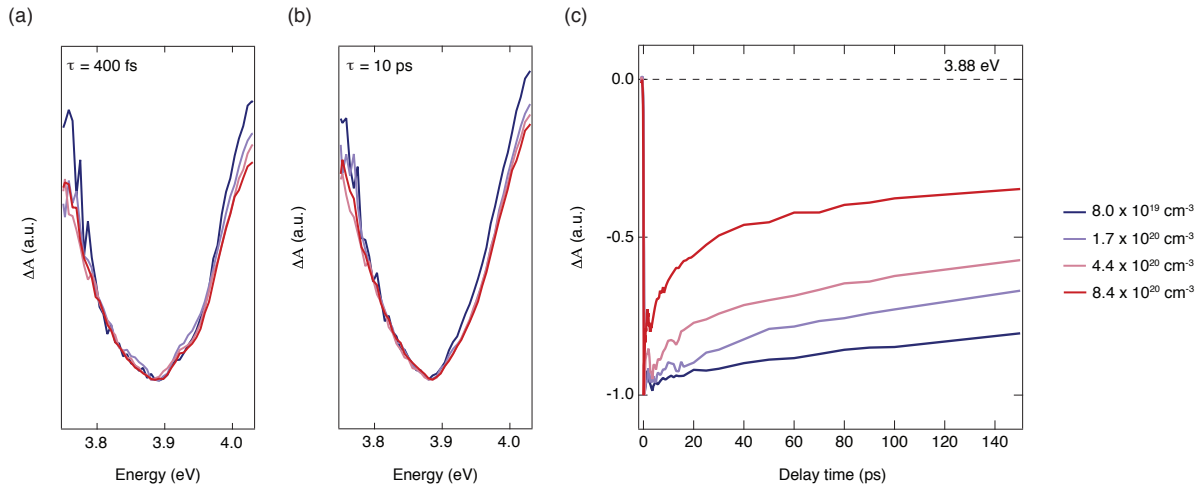

FIG. 4. (a,b) Normalized ΔA spectra as a function of probe photon energy for different photoexcited carrier densities. Spectra in (a) are cut at a delay time of 400 fs, spectra in (b) at 10 ps. (c) Normalized temporal traces at 3.88 eV for different photoexcited carrier densities.

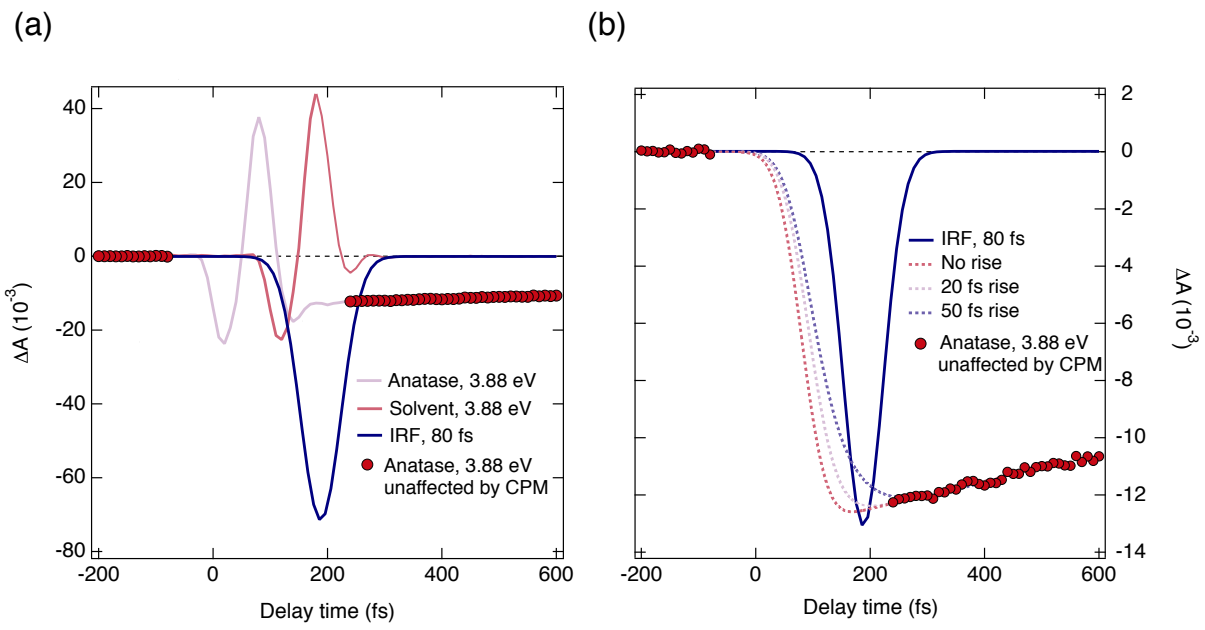

FIG. 5. (a) Comparison between the ΔA signal from the colloidal solution of anatase TiO_2 and the ΔA signal from the solvent alone. The ΔA response of anatase TiO_2 unaffected by CPM and the Gaussian instrument response function (of 80 fs) are also reported. (b) Evaluation of the rise-time of the ΔA signal by comparison of the ΔA response of anatase TiO_2 (unaffected by CPM) with three different decay functions (convoluted with a Gaussian instrument response function of 80 fs).

S1. Sample preparation

The TiO_2 nanoparticles (NPs) were prepared using the sol-gel method [45]. The synthesis was carried out in a glove box under argon atmosphere. Titanium isopropoxide (Sigma Aldrich, 99.999% purity) was used as precursor and was mixed with 10 ml of 2-propanol. This mixture was added dropwise under vigorous stirring to cold acidic water (2 °C, 250 ml H_2O, 18 MΩ, mixed with 80 ml glacial acetic acid, final pH 2). At the beginning the mixture looked turbid, but after stirring it in an ice bath for 12 hours, it became transparent as the amorphous NPs were formed. The mixture was then peptized at 80 °C for about 2 hours until the liquid turned into a transparent gel. The gel was autoclaved at 230 °C for 12 hours. During this process the previous amorphous TiO_2 sample became denser and underwent a phase transition, resulting in anatase TiO_2 NPs. After the autoclave, the NPs have precipitated to the bottom of the container. They were separated from the supernatant and added to 100 ml acidic water (pH 2) to obtain a white colloidal solution with a final concentration of ca. 5 g/L. In Ref. [46], we reported the details of the sample characterization by means of x-ray diffraction and Transmission Electron Microscopy. Using these techniques, the good quality of the anatase phase and the spherical shape (with an average diameter of approximately 25 nm) of the NPs were demonstrated. The steady-state absorption specta reported in Fig. S1 were recorded at room temperature using a commercial spectrometer (Shimadzu, UV-3600). Before measuring the absorption spectrum of the sample, a reference spectrum of the pure solvent (acidic water, pH 2) was taken to check its transparency in the investigated spectral range.

S2. Ultrafast two-dimensional deep-ultraviolet spectroscopy

The ultrafast two-dimensional (2D) deep-ultraviolet (UV) spectroscopy measurements have been performed using a set-up described in detail in Ref. [32]. Briefly, a 20 kHz Ti:Sapphire regenerative amplifier (KMLabs, Halcyon + Wyvern500), providing pulses at 800 nm (1.55 eV), with typically 0.6 mJ energy and around 50 fs duration, pumps a non-collinear optical parametric amplifier (NOPA) (TOPAS white - Light Conversion) to generate sub-90 fs visible pulses (1.77 - 2.30 eV range). The typical output energy per pulse is 13 μJ. Around 60% of the output of the NOPA is used to generate the narrowband pump

pulses. The visible beam, after passing through a chopper, operating at 10 kHz and phase-locked to the laser system, can be focused onto a 2 mm thick barium borate (BBO) crystal for obtaining the UV pump pulse. In this case, the pump photon energy is controlled by the rotation of the crystal around the ordinary axis and can be tuned in a spectral range up to $\geq$ 0.9 eV ($\geq$ 60 nm) wide. The typical pump bandwidth is 0.02 eV (1.5 nm) and the maximum excitation energy is about 120 nJ. The pump power is recorded on a shot-to-shot basis by a calibrated photodiode for each pump photon energy, allowing for the normalization of the data for the pump power. The remaining NOPA output is used to generate the broadband UV probe pulses with $\geq$ 100 nm bandwidth through an achromatic doubling scheme. Pump and probe pulses, which have the same polarization, are focused onto the sample, where they are spatially and temporally overlapped. The typical spot size of the pump and the probe are 100 $\times$ 150 μm^2 and 40 $\times$ 44 μm^2 full-width half-maximum (FWHM) respectively, resulting in a homogeneous illumination of the probed region.

For most measurements, the colloidal solution circulated into a 0.2 mm thick quartz flow-cell to prevent photo-damage and its concentration was adjusted to provide an optical density of approximately 0.4 at the pump photon energy of 4.05 eV. Alternatively, for limiting the issues of cross-phase modulation in the sample and achieving a better time resolution, the NPs solution could be made flowing in the form of 0.2 mm thick jet. The probe was measured after its transmission through the sample and its detection synchronized with the laser repetition rate. The difference of the probe absorption with and without the pump pulse has been measured at varying time delays between the pump and the probe, thanks to a motorized delay line in the probe path. After the sample, the transmitted broadband probe beam was focused in a multi-mode optical fiber (100 μm), coupled to the entrance slit of a 0.25 m imaging spectrograph (Chromex 250is). The beam was dispersed by a 150 gr/mm holographic grating and imaged onto a multichannel detector consisting of a 512 pixel CMOS linear sensor (Hamamatsu S11105, 12.5 $\times$ 250 μm pixel size) with up to 50 MHz pixel readout, so the maximum read-out rate per spectrum (almost 100 kHz) allowed us to perform shot to-shot detection easily. The experimental setup offered a time resolution of 150 fs, but this could be improved to 80 fs with the adoption of a prism compressor on the pump pulses, at the expenses of a reduction of the probe bandwidth in the achromatic frequency doubling scheme.

To study the response of the anatase TiO_2 NPs at high fluence upon excitation at 3.10

eV, we also used another visible pump/deep-UV continuum probe setup, described in Ref. [47]. Briefly, a 1 kHz regenerative amplifier provides 30 fs pulses at 800 nm (1.55 eV) with a pulse energy of 620 μJ. Part of the beam is focused onto a 2 mm thick BBO crystal for obtaining the 400 nm (3.10 eV) pump pulse. The remaining part of the regenerative amplifier output is used to pump one home-built NOPA, which deliver typical pulses of 1-2 μJ and 80 nm bandwidth at 600 nm, with a pulse duration of about 30 fs. The output of the NOPA is used to generate a broadband UV pulse via achromatic doubling in a 0.15 mm thick BBO crystal. The experimental scheme here is quite different from the one described above, and the bandwidth of the generated broadband pulses is narrower. Three separate experiments are necessary to fully cover the 3.20-4.60 eV spectral region. After the sample, the probe beam is dispersed by an 830 gr/mm transmission grating and focused on a 512 pixel photodiode array. Typical pump and probe focus dimensions are 120 μm and 60-80 μm.

S3. Ultrafast broadband fluorescence upconversion

The ultrafast broadband fluorescence upconversion measurements have been performed using a set-up described in detail in Ref. [48]. In our experimental configuration, a 150 kHz Ti:Sapphire regenerative amplifier system (Coherent, RegA-9000) is seeded by a mode-locked Ti:Sapphire oscillator (Coherent, Mira-SEED) and produces 4 μJ pulses at 800 nm (1.55 eV) with a 80 fs pulse width. The beam is then split into two arms with a pellicle beam splitter: The reflected part is used for gating, the remaining for generating the pump beam at 266 nm (4.66 eV) via frequency tripling. The excitation light is focused with an area of 35 μm of diameter onto a 0.2 mm thick quartz flow-cell, in which the colloidal solution of anatase TiO_2 circulates continuously. The light emitted by the sample is collected by a parabolic mirror in forward-scattering geometry, and directed to a second mirror that focuses it onto a BBO crystal for sum frequency generation. The luminescence is then up-converted by mixing with the gate pulse in a slightly non-collinear geometry. The up-converted signal is spatially filtered and detected with a spectrograph and a liquid nitrogen cooled charge-coupled device camera. The experimental setup offers a time resolution of 150 fs.

S4. Estimation of the carrier density

We calculate the number of excited electron-hole pairs per unit cell of anatase TiO_2 by taking into account a sample of NPs, flowing in a quartz flow cell of thickness $l = 0.2$ mm with a concentration of $c = 0.106$ g/L and an optical density of $OD = 0.4$. Specifically, we consider the ultrafast broadband deep-UV experiment in which the sample is pumped with a photon energy $E_{pump} = 4.05$ eV at a repetition rate of $f = 20$ kHz and average power P. This calculation can be easily extended for the other experimental parameters used in this work.

The energy per pulse is $E_{pulse} = P/f$, corresponding to a number of photons per pulse of $N_{pulse} = E_{pulse}/E_{ph}$. The pump is focused on an area of $A_{foc} = \pi \times 50\ \mu m \times 75\ \mu m = 1.18 \times 10^{-8}\ m^2$, corresponding to a focusing volume of $V_{pump} = A_{foc}l = 2.36 \times 10^{-12}\ m^3$. Since the radius of one NP is $R \sim 14$ nm, the volume can be estimated by approximated the NP to a sphere. This yields $V_{np} = \frac{4}{3}\pi R^3 = 1.15 \times 10^{-23}\ m^3$. The anatase TiO_2 density is $\rho = 3.9\ 10^6\ g/m^3$ and the mass of one NP is $M_{np} = V_{np}\rho = 4.5 \times 10^{-17}$ g. Given the concentration c, the number of NPs in the volume where the pump beam is focused is $N_{foc} = cV_{pump}10^3/M_{np} = 5.57 \times 10^6$. The number of photons absorbed in a pulse is $N_{abs} = (1 - T)N_{pulse}$, where $T = 10^{-OD} = 0.398$. In conclusion, the photoexcited carrier density n is calculated as the ratio between total number of absorbed photons and the total illuminated volume $N_{foc} \times V_{pump}$.

S4. Indirect bandgap photoexcitation

We also perform a separate ultrafast broadband deep-UV experiment to verify the appearance of the a-axis exciton feature when the pump beam is tuned within the spectral region of indirect interband transitions. These transitions involve the phonon-assisted generation of electron-hole pairs in the material. While the electrons are promoted in the region around the Γ point of the conduction band, the holes are expected to be located in the valence band at the X and Z valleys of the Brillouin zone. As such, the cross section of these transitions is rather low. Spectrally, the region of phonon-assisted interband transitions extends from the indirect bandgap energy 3.20 eV to the direct exciton feature and, as such, it lies below the excitation region explored in the 2D deep-UV measurements. To this aim, in this separate

experiment, we tune our pump photon energy to 3.54 eV and measure the ΔA response of the anatase TiO_2 colloidal solution in the vicinity of the a-axis exciton peak (3.70 - 4.10 eV). The photoexcited carrier density is estimated around 1×10^{19} cm^{-3}, which yield a very weak ($\Delta A \sim 10^{-3}$) signal. The colour-coded map of ΔA as a function of probe photon energy and time delay between pump and probe is shown in Fig. S2. We clearly distinguish the a-axis exciton bleach persisting up to 1 ns.

S5. Choice of the electron effective mass

The electron effective mass was recently measured via ARPES to be around $m_e^* = 0.7m_e$ (where m_e is the bare electron mass) for excess carrier densities $n \sim 10^{18} \div 10^{19}$ cm^{-3} [9], which is larger than the one predicted by band structure calculations ($m_e^* = 0.42m_e$ [39]) due to the polaronic dressing of the electrons. For higher carrier density regimes, m_e^* is expected to decrease towards the values predicted by band structure calculations due to an effective screening of the electron-phonon interaction [9]. Thus, in Eqs. (2)-(3) of the main text, we make use of the value reported by band theory.

S6. Ultrafast photoluminescence of anatase TiO_2 nanoparticles

To establish the nature of the mechanisms governing the recombination dynamics in anatase TiO_2 NPs, we perform ultrafast broadband fluorescence upconversion. Our aim is to determine whether radiative (bimolecular) recombination processes take place at room temperature within the first 100 ps and, in this case, to evaluate the effective photoluminescence (PL) quantum yield for such processes. In the past, a number of works studied the radiative decay in anatase TiO_2 single crystals, thin films and NPs, both at low and room temperature [12–18, 49]. Since anatase TiO_2 is an indirect bandgap insulator, band-to-band radiative recombination processes are unlikely, as the photoluminescence process requires phonon emission to conserve momentum. As such, the PL response in anatase TiO_2 is dominated by other sources of radiative recombination. More specifically: i) the intrinsic PL from the radiative recombination of self-trapped excitons; ii) the extrinsic PL from the radiative decay at impurities and defects. As both contributions give rise to broad PL signals covering the visible range, a distinction can be made depending on the central PL photon

energy. Intrinsic PL from self-trapped excitons is prominent at low temperature and shows a large Stokes-shift with respect to the indirect absorption threshold of the material. This PL band is centered around 2.37 eV at low temperature and undergoes a sizeable blueshift for increasing temperature, reaching 2.57 eV at 300 K. In contrast, broad PL signals from defects show less pronounced temperature dependence for their central peak, being centered around 2.24 eV. Interestingly, no studies of the ultrafast PL in the first 100 ps of the response have been reported yet. Hence, it is still an open question whether the system undergoes radiative recombination pathways during these short timescales. An estimate of the PL quantum yield would also clarify the origin of the high order recombination processes observed in the ultrafast 2D deep-UV data.

To this aim, here we perform ultrafast broadband fluorescence upconversion measurements on the same colloidal solution of anatase TiO_2 NPs used for the ultrafast 2D deep-UV spectroscopy study. As it is well established that the spectral content of the PL response does not depend on the pump photon energy for above-gap excitation, in our study we employ a pump pulse centered around 4.66 eV. The broad PL spectrum at a time delay of 1 ps is shown in Fig. S3(a). The PL appears only in the visible regime and is completely absent in the spectral region > 3.00 eV. It retains the form of a broad band centered around 2.24 eV, which is characterized by an extremely weak intensity. Figure S3(b) displays the temporal traces at 1.91 eV, 2.18 eV and 2.58 eV. The PL signal rises within our experimental temporal resolution (200 fs) and decays bi-exponentially with time constants of 2 ps and 30-40 ps.

Since the PL band is centered around 2.24 eV, we assign it to an extrinsic radiative recombination channel that involves carriers trapped at defect states. A detailed study of the origin of this ultrafast PL response will be subject of a future work. Here we are only interested in ruling out any involvement of radiative decay channels in the recovery of the exciton bleach signal shown in the main text. Thus, irrespective of the origin (intrisic vs. extrinsic) of the PL band, we evaluate the PL quantum yield for time delays below 500 ps. By considering that the whole PL band observed in our experiment yields 3.6×10^9 emitted photons per second. This value has to be compared with the number of absorbed photons per second by the whole colloidal anatase TiO_2 solution, which amounts to 2.8×10^{15}. Thus, we estimate a quantum yield of $\sim 1.3 \times 10^{-6}$. This is consistent with the fact that the quantum yield of anatase TiO_2 NPs at room temperature and under steady-state

conditions has been found $\sim 2.5 \times 10^{-3}$ [50, 51]. Indeed, the latter represents an upper limit to the PL quantum yield that can be obtained in anatase TiO_2 NPs at room temperature and, as expected, it implies that the radiative decay channel is not efficient in this material.

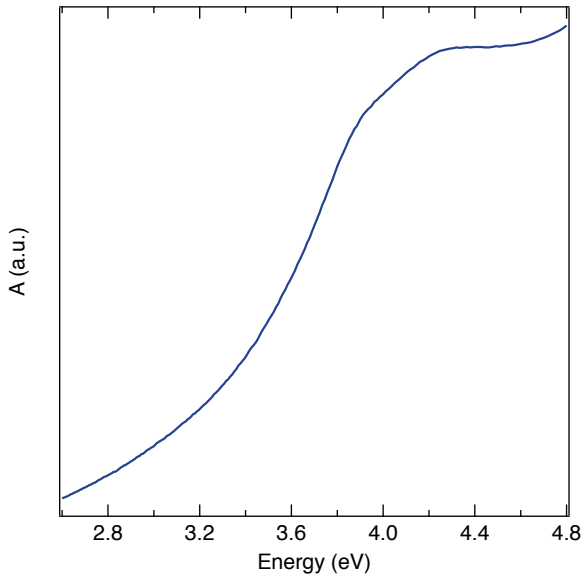

FIG. S1. Room temperature steady-state absorption spectrum of anatase TiO_2 NPs dispersed in aqueous solution.

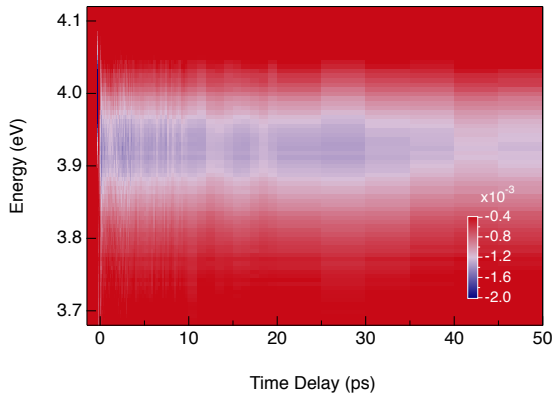

FIG. S2. Colour-coded map of ΔA measured on a colloidal solution of anatase TiO_2 NPs at room temperature as a function of probe photon energy and time delay between pump and probe. The time resolution is estimated 150 fs, the pump photon energy is set at 3.54 eV and the delivered pump fluence is 100 $\mu J/cm^2$.

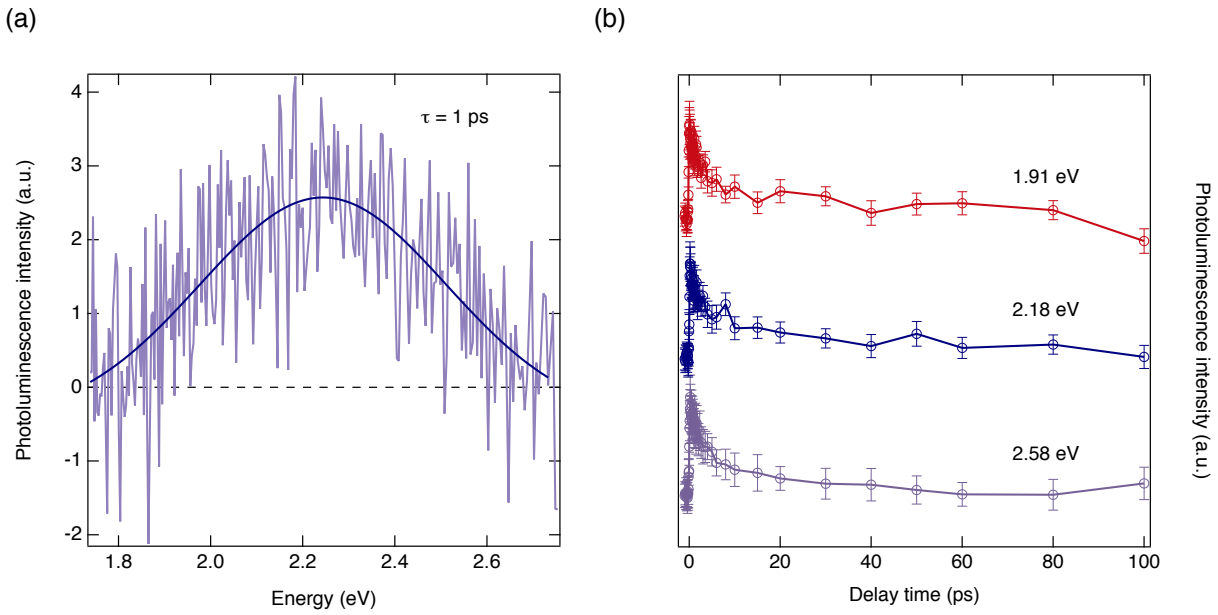

FIG. S3. (a) Experimental spectrum of the ultrafast PL at a time delay of 1 ps (violet curve) and gaussian fit of the response (blue curve). (b) Temporal evolution of the ultrafast PL at 1.91 eV (red curve), 2.18 eV (blue curve) and 2.58 eV (violet curve).

[1] A. Fujishima and K. Honda, Nature **238**, 37 (1972).

[2] E. Pelizzetti and C. Minero, Electrochimica Acta **38**, 47 (1993).

[3] B. O. Reagen and M. Grätzel, Nature **353**, 737 (1991).

[4] P. A. Cox, *Transition metal oxides: an introduction to their electronic structure and properties*, Vol. 27 (Oxford university press, 2010).

[5] H. Tang, F. Levy, H. Berger, and P. E. Schmid, Phys. Rev. B **52**, 7771 (1995).

[6] N. A. Deskins and M. Dupuis, Phys. Rev. B **75**, 195212 (2007).

[7] C. Di Valentin and A. Selloni, J. Phys. Chem. Lett. **2**, 2223 (2011).

[8] J. Jaćimović, C. Vaju, A. Magrez, H. Berger, L. Forró, R. Gaal, V. Cerovski, and R. Žikić, EPL Europhys. Lett. **99**, 57005 (2012).

[9] S. Moser, L. Moreschini, J. Jaćimović, O. S. Barišić, H. Berger, A. Magrez, Y. J. Chang, K. S. Kim, A. Bostwick, and E. Rotenberg, Phys. Rev. Lett. **110**, 196403 (2013).

[10] M. Setvin, C. Franchini, X. Hao, M. Schmid, A. Janotti, M. Kaltak, C. G. van de Walle, G. Kresse, and U. Diebold, Phys. Rev. Lett. **113**, 086402 (2014).

[11] V. P. Zhukov and E. V. Chulkov, Phys. Sol. State **56**, 1302 (2014).

[12] H. Tang, H. Berger, P. E. Schmid, F. Levy, and G. Burri, Sol. State Comm. **87**, 847 (1993).

[13] M. Watanabe, S. Sasaki, and T. Hayashi, J. Lumin. **87**, 1234 (2000).

[14] M. Watanabe and T. Hayashi, J. Lumin. **112**, 88 (2005).

[15] K. Wakabayashi, Y. Yamaguchi, T. Sekiya, and S. Kurita, J. Lumin. **112**, 50 (2005).

[16] N. Harada, M. Goto, K. Iijima, H. Sakama, N. Ichikawa, H. Kunugita, and K. Ema, Jpn. J. Appl. Phys. **46**, 4170 (2007).

[17] L. Cavigli, F. Bogani, A. Vinattieri, V. Faso, and G. Baldi, J. Appl. Phys. **106**, 053516 (2009).

[18] L. Cavigli, F. Bogani, A. Vinattieri, L. Cortese, M. Colocci, V. Faso, and G. Baldi, Solid State Sciences **12**, 1877 (2010).

[19] E. Baldini, L. Chiodo, A. Dominguez, M. Palummo, S. Moser, M. Yazdi, G. Auböck, B. P. P. Mallett, H. Berger, A. Magrez, *et al.*, arXiv preprint arXiv:1601.01244 (2016).

[20] H. M. Lawler, J. J. Rehr, F. Vila, S. D. Dalosto, E. L. Shirley, and Z. H. Levine, Phys. Rev. B **78**, 205108 (2008).

[21] L. Chiodo, J. M. García-Lastra, A. Iacomino, S. Ossicini, J. Zhao, H. Petek, and A. Rubio,

Phys. Rev. B **82**, 045207 (2010).

[22] W. Kang and M. S. Hybertsen, Phys. Rev. B **82**, 085203 (2010).

[23] M. Landmann, E. Rauls, and W. G. Schmidt, J. Phys. Condens. Matter **24**, 195503 (2012).

[24] Y. Toyozawa, *Optical processes in solids* (Cambridge University Press, 2003).

[25] D. P. Colombo, K. A. Roussel, J. Saeh, D. E. Skinner, J. J. Cavaleri, and R. M. Bowman, Chem. Phys. Lett. **232**, 207 (1995).

[26] A. Furube, T. Asahi, H. Masuhara, H. Yamashita, and M. Anpo, J. Phys. Chem. B **103**, 3120 (1999).

[27] X. Yang and N. Tamai, Phys. Chem. Chem. Phys. **3**, 3393 (2001).

[28] Y. Tamaki, A. Furube, R. Katoh, M. Murai, K. Hara, H. Arakawa, and M. Tachiya, Cr. Chim. **9**, 268 (2006).

[29] Y. Tamaki, K. Hara, R. Katoh, M. Tachiya, and A. Furube, J. Phys. Chem. C **113**, 11741 (2009).

[30] Y. Yamada and Y. Kanemitsu, Appl. Phys. Lett. **101**, 133907 (2012).

[31] H. Matsuzaki, Y. Matsui, R. Uchida, H. Yada, T. Terashige, B.-S. Li, A. Sawa, M. Kawasaki, Y. Tokura, and H. Okamoto, Jpn. J. Appl. Phys. **115**, 053514 (2014).

[32] G. Auböck, C. Consani, F. van Mourik, and M. Chergui, Opt. Lett. **37**, 2337 (2012).

[33] H. Haug and S. Schmitt-Rink, JOSA B **2**, 1135 (1985).

[34] S. Schmitt-Rink, D. S. Chemla, and D. A. B. Miller, Adv. Phys. **38**, 89 (1989).

[35] N. Serpone, D. Lawless, and R. Khairutdinov, J. Phys. Chem. **99**, 16646 (1995).

[36] S. Das Sarma and D. W. Wang, Phys. Rev. Lett. **84**, 2010 (2000).

[37] P. T. Landsberg, *Recombination in Semiconductors* (Cambridge University Press, 2003).

[38] E. M. Bothschafter, A. Paarmann, E. S. Zijlstra, N. Karpowicz, M. E. Garcia, R. Kienberger, and R. Ernstorfer, Phys. Rev. Lett. **110**, 067402 (2013).

[39] T. Hitosugi, H. Kamisaka, K. Yamashita, H. Nogawa, Y. Furubayashi, S. Nakao, N. Yamada, A. Chikamatsu, H. Kumigashira, M. Oshima, *et al.*, Appl. Phys. Exp. **1**, 111203 (2008).

[40] H. Fröhlich, H. Pelzer, and S. Zienau, The London, Edinburgh, and Dublin Philosophical Magazine and Journal of Science **41**, 221 (1950).

[41] J. Van Mechelen, D. Van der Marel, C. Grimaldi, A. Kuzmenko, N. Armitage, N. Reyren, H. Hagemann, and I. Mazin, Phys. Rev. Lett. **100**, 226403 (2008).

[42] R. Gonzalez, R. Zallen, and H. Berger, Phys. Rev. B **55**, 7014 (1997).

[43] E. Hendry, F. Wang, J. Shan, T. F. Heinz, and M. Bonn, Phys. Rev. B **69**, 081101 (2004).

[44] U. Bockelmann and G. Bastard, Phys. Rev. B **42**, 8947 (1990).

[45] S. Mahshid, M. S. Ghamsari, M. Askari, N. Afshar, and S. Lahuti, Semiconductor Physics, Quantum Electronics & Optoelectronics **9**, 65 (2006).

[46] M. H. Rittmann-Frank, C. J. Milne, J. Rittmann, M. Reinhard, T. J. Penfold, and M. Chergui, Angewandte Chemie International Edition **53**, 5858 (2014).

[47] C. Consani, M. Prémont-Schwarz, A. ElNahhas, C. Bressler, F. van Mourik, A. Cannizzo, and M. Chergui, Angewandte Chemie International Edition **48**, 7184 (2009).

[48] A. Cannizzo, O. Bräm, G. Zgrablic, A. Tortschanoff, A. A. Oskouei, F. van Mourik, and M. Chergui, Optics letters **32**, 3555 (2007).

[49] J. Preclíková, P. Galář, F. Trojánek, S. Daniš, B. Rezek, I. Gregora, Y. Němcová, and P. Malỳ, J. Appl. Phys. **108**, 113502 (2010).

[50] N. D. Abazović, M. I. Čomor, M. D. Dramićanin, D. J. Jovanović, S. P. Ahrenkiel, and J. M. Nedeljković, The Journal of Physical Chemistry B **110**, 25366 (2006).

[51] N. D. Abazović, I. A. Ruvarac-Bugarčić, M. I. Čomor, N. Bibić, S. P. Ahrenkiel, and J. M. Nedeljković, Optical Materials **30**, 1139 (2008).